Mechanisms of electrochemical magnesium (de)alloying of Mg-Sn and Mg-Pb polymorphs

Clément Pechberty, Antoine Klein, Bernard Fraisse, Lorenzo Stievano, Romain Berthelot

Electrochemical behavior of Mg_2Sn and Mg_2Pb polymorphs in Mg-ion batteries

Submission to Journal of Magnesium and Alloys

Clément Pechberty, Antoine Klein, Bernard Fraisse, Lorenzo Stievano, Romain Berthelot*

ICGM, Univ Montpellier, CNRS, ENSCM, Montpellier, France

RS2E, CNRS, Hub de l'Energie, Amiens, France

Corresponding author

Dr. Romain Berthelot

romain.berthelot@umontpellier.fr

Institut Charles Gerhardt de Montpellier – CC1502

Université de Montpellier – Campus Triolet

2, place Bataillon – 34095 Montpellier - France

Highlights

- Polymorphs of Mg_2Sn and Mg_2Pb are prepared by high-energy ball-milling and evaluated in magnesium-ion cells.
- The alloying/de-alloying process is analyzed by *operando* X-ray diffraction
- The alloying process favors the formation of the cubic alloy for both tin and lead

Abstract

Cubic and non-cubic polymorphs of Mg_2Sn and Mg_2Pb have been evaluated as electrode materials for magnesium-ion batteries. The intermetallic compounds have been prepared by high-energy ball-milling and characterized by X-ray powder diffraction and scanning electron microscopy. The alloying electrochemical mechanism has been investigated by *operando* X-ray diffraction supported by a data analysis chemometric approach. For both tin and lead, the alloying process tends to form the cubic polymorphs, with sometimes traces of the non-cubic form in the first moments of the electrochemical magnésiation. Finally, the compatibility of Mg_2Sn and Mg_2Pb with $Mg(TFSI)_2$-based electrolyte is confirmed in full cell with Chevrel phase Mo_6S_8 positive electrode material.

Keywords

Alloy electrode, mechanochemistry, operando measurements, X-ray diffraction, Magnesium battery

1. Introduction

Magnesium batteries are currently investigated as a possible alternative to the well-established lithium-ion technology.[1,2] Driven by the growing market of electric vehicles, the increasing demand for batteries could indeed face some sustainability issues regarding specific raw materials, such as cobalt, nickel or lithium. It is thus important to investigate other types of batteries employing more abundant elements such as magnesium. The story of rechargeable magnesium batteries really started with the prototype systems of Aurbach, with the Chevrel phase Mo_6S_8 at the positive electrode, a magnesium metal negative electrode and Grignard-

based electrolytes.[3] This pioneering work already underlined the two major challenges of the Mg-batteries: the easy surface passivation of the magnesium in contact with conventional electrolytes classically used for battery and the lack of positive electrode materials due to the sluggish ionic diffusion of Mg^{2+} into classical host electrodes.[4,5] Tremendous efforts have been made to identify new generations of electrolytes suitable for a magnesium electrode, and more practical than the Grignard-based ones (simpler, less corrosive and with a wider electrochemical stability window). At the positive electrode, sulfur-based composites seem to focus nowadays most of the attention.[6] Indeed, the conversion process leading to magnesium sulfide MgS is reversible and induces high capacities. The theoretical combination of magnesium and sulfur in a same battery would offer high energy density above 3200 Wh/L, while being sustainable and affordable. However, such a promising system would also come along with the well-known drawbacks of metal/sulfur systems (insulating nature of sulfur implying limited loading in the electrode, polysulfide shuttle effect, *etc.*).[6]

Recently, the spotlight has been focused on alloy-type electrodes for magnesium-ion systems, thanks to the relatively high theoretical capacity and the low alloying potentials of elements from groups IIIA, IVA and VA. Bismuth, antimony were the first alloy-type electrodes investigated in magnesium-ion batteries, followed by reports on silicon, germanium, tin, indium and more recently gallium.[7] Obviously, most of the studies evaluated these elements in half-cell configuration with magnesium counter electrode and Grignard-based electrolytes. However, the compatibility with more conventional and practical electrolytes has been rapidly underlined and stands now as the main advantage of these alloy-type electrodes. Consequently, the use of magnesium alloy Mg_xM has been proposed to investigated Mg-free positive electrode materials, like the Chevrel phase standard Mo_6S_8, but also vanadium oxide V_2O_5 or carbon/sulfur composites, in simple electrolyte generally made from $Mg(TFSI)_2$ salt dissolved in acetonitrile, tetrahydrofuran or dimethoxyethane.[8–10]

Among the different Mg_xM alloy systems, promising results can be predicted for Sn- and Pb-based alloys based on the behavior of these metals as alloy-type negative electrodes. Concerning tin, during the first investigation of its electrochemical behavior in magnesium batteries, Singh *et al.* observed at C/200 an alloying plateau around 0.15 V ending with a high discharge capacity of 900 mAh/g_{Sn}, *i.e.*, close to the theoretical value corresponding to the formation of Mg_2Sn. However, they also showed that magnesiated electrodes further deliver a fraction of this initial capacity (~300 mAh/g_{Sn}).[11] Irreversible pulverization and amorphization upon cycling could explain this limited capacity. The electrochemical behavior of bulk Mg_2Sn prepared by ball-milling was then investigated by Nguyen and coworkers. After initial capacity below 200 mAh/g_{Mg2Sn} a maximum of 270 mAh/g_{Mg2Sn} was reached upon cycling. Galvanostatic intermittent titration technique, or optimized electrode formulation, enabled reaching higher values.[12,13]

In the case of lead, its electrochemical behavior was investigated in 2015 by the group of Obrovac, starting from electrodes either prepared by sputtering or made from micrometric Pb powder.[14] At 60°C and current rates of C/40 or C/50, reversible capacities of 450 and 275 mAh/g_{Pb} were obtained, respectively, with Grignard-based electrodes. The alloying process occurs at 125 mV *vs.* Mg. Only indium-based electrodes exhibit a lower alloying potential. To bypass an initial catalytic reaction on the electrode surface, the application of a current pulse prior to the discharge was proposed. To the best of our knowledge, no investigation of the electrochemical behavior of Mg_2Pb has been performed until now.

In this current work, the electrochemical behavior of intermetallic compounds around the Mg_2Sn and Mg_2Pb compositions prepared by mechanical alloying is investigated. In particular, *operando* X-ray diffraction is used to follow the corresponding electrochemical processes. Lastly, compatibility with conventional electrolyte is also demonstrated by assembling full cells with a Chevrel phase positive electrode.

2. Experimental

Magnesium, tin and lead powders (Sigma-Aldrich, 99%, 325 mesh, Alfa Aesar, 99.5%, 100 mesh and 98%, 20–230 mesh, respectively) were used as received and mixed in a 3D Spex mill (Spex SamplePrep 8000 M) in argon atmosphere with stainless steel jar and balls. For typically 1 g of powders mixture, 4 grinding balls of 10 mm diameter are used. The nominal powders proportions varied around the stoichiometric 2:1 ratio.

The resulting materials were then characterized by X-ray powder diffraction (XRPD) with a Panalytical X'Pert Pro diffractometer operating with Cu Kα radiation, under a protective airtight polymeric film to limit moisture reaction. Powder morphology was also observed by scanning electron microscopy (SEM) with a Hitachi S-4800 microscope.

Self-supported electrodes were prepared in a mortar by mixing 70 wt.% of active powder (Mg_2Pb or Mg_2Sn), 10 wt.% of carbon (C65, Timcal), 10wt% of vapor grown carbon fibers (VGCF-H, Showa Denko K.K.) and 10 wt.% of polytetrafluoroethylene (PTFE, Sigma-Aldrich, >40µm). The paste obtained was punch into disc to form 8mm diameter electrodes with an average mass loading of 30 mg/cm². All these operations were made in an argon-filled glove box (MBraun LABSTAR) with an oxygen level <0.5 ppm.

Chevrel phase Mo_6S_8 was synthetized by adapting widely accepted 2-step protocol.[15] Firstly, the ternary $Cu_{2.5}Mo_6S_8$ Chevrel phase was obtained by heating a stoichiometric mixture of Cu (Sigma-Aldrich, 99.9%, 325 mesh), Mo (Alfa-Aesar, 99.95%, APS 3.7µm) and MoS_2 (Sigma-Aldrich, 99%, <2µm) during 24 hours at 1000 °C under constant argon flow. Secondly, Cu was removed by acidic leaching with HCl aqueuous solution (6 M) under bubbling O_2. Finally, the solid was filtered, washed with distilled water and ethanol and lastly dried at 60 °C. The final product was characterized by XRPD to check the purity of the obtained

Chevrel phase. Mo_6S_8 electrodes film were formulated by mixing 80 wt.% of Mo_6S_8, 5 wt.% of C65, 5 wt.% of VGCF-H, 10% of polyvinylidene fluoride (PVDF, SOLEF 21216/1001) and NMP as the solvent. The slurry was then tape-casted on 10 µm carbon-coated aluminum foil and dried following the above-mentioned procedure, leading to electrodes with an average mass loading around 1.5 mg/cm².

All-ethyl-complex magnesium electrolyte (AEC) was obtained by mixing ethylmagnesium chloride (EtMgCl, 2M in THF, Sigma –Aldrich) and diethylaluminium chloride (Et_2AlCl, 97% Sigma-Aldrich) in THF. The final concentration of the EtMgCl-Et_2AlCl-THF electrolyte is around 0.35 M. Conventional magnesium electrolyte was prepared by dissolving magnesium bis(trifluoromethanesulfonyl)imide salt ($Mg(TFSI)_2$, 99.5%, Solvionic) in dimethoxethane (DME, Sigma-Aldrich purity > 99 %)) with a 0.5 M concentration. Prior to use, $Mg(TFSI)_2$ was dried at 250°C in a vacuum flask, while DME was dried first by argon bubbling, then by addition of 4 Å molecular sieves for 3 days, next refluxed with K/Na (3/1 wt.%) for 1 day and finally distilled.

2-electrode coin-cells (2032, 316L stainless steel) were assembled in an argon-filled glove-box, with Mg disks (Goodfellow, 99.9%, 250 µm) as both the negative and reference electrode. Two Whatman GF/A borosilicate glass fibers were used as separator and wetted with 100 µL of electrolyte. All Galvanostatic tests was perform on an MPG potentiostats (Biologic).

Operando XRD measurements were carried out on an electrochemical cell with a specific Be window to probe the structural evolution of the electrode material.[16] Mg disc and Mg_2Pb self-supported electrode were used as negative/reference and positive electrode, respectively. The current rate was C/25 during the charge and the start of the discharge, then a constant potential was applied to force the discharge to continue.

3. Results and Discussion

The XRPD patterns obtained after mechanical alloying of Mg-Sn and Mg-Pb mixtures with various stoichiometries around Mg_2M and milling times are gathered in Figure 1. In 5 hours and with a molar magnesium excess of 10 %, the cubic phases Mg_2Sn and Mg_2Pb are obtained. The patterns exhibits well-defined diffraction patterns that can be indexed with the cubic space group *Fm*-3*m*. The corresponding refined cell parameters are in good agreement with the literature (a = 6.762(2) Å for Mg_2Sn, a =6.820(1) Å for Mg_2Pb, Figure S1). For longer milling times, and/or with lower amounts of magnesium, the patterns significantly change and early-stage phase searching did not provide a unique solution (Fig. 1b and 1d). Consequently, it is important to detail the equilibrium phase diagrams of the Mg-Sn and Mg-Pb systems. If cubic Mg_2Sn and Mg_2Pb, crystallizing in the antifluorite-type structure,[17,18] are reported as the thermodynamically stable allotropes at ambient conditions, other polymorphs are known in a narrow region around Mg_2Sn and Mg_2Pb compositions.

For the Mg-Sn system, an hexagonal phase was reported firstly at high-pressure and high-temperature,[19,20] but then also through long-time mechanical alloying.[21] A slight Mg-deficient composition, Mg_9Sn_5, was later proposed for this dense form with the hexagonal cell parameters a = 13.222 Å and c = 13.15 Å.[22] Also through ball-milling, a metastable phase with an orthorhombic structure was detected by Clark *et al.* with cell parameters a = 15.23 Å, b = 8.90 Å and c = 13.10 Å,[23] on the basis of a first example on thin film obtained by metal evaporation.[24] Profile matching was attempted with both the orthorhombic and the hexagonal models. Owing to the quite broad diffraction peaks (usually obtained with mechanochemical alloying), however, the refinements were not satisfactory enough to clearly discriminate between the two models. Consequently, this polymorph will be hereafter named "non-cubic Mg_2Sn".

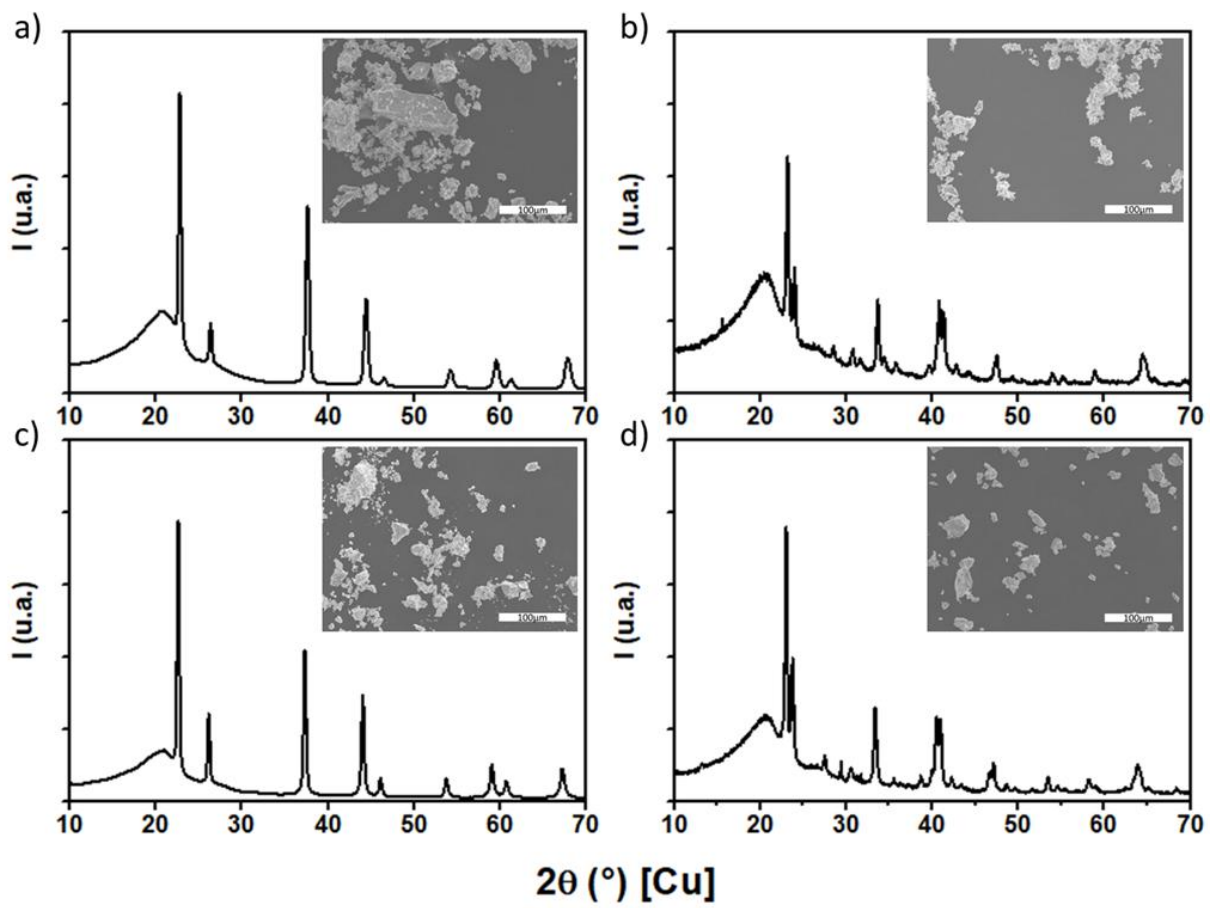

Figure 1: XRPD patterns and SEM pictures of Mg_2Sn cubic (a) and non-cubic (b) and Mg_2Pb cubic (c) and non-cubic (d). Scale bar is 100 µm. For the cubic polymorphs, profile matching refinement is provided in supplementary section.

Regarding the Mg-Pb system, in 1965 Eldrige *et al.* showed that cubic Mg_2Pb melts incongruently and forms a β' phase at a different composition slightly deficient in Mg.[25] This polymorph was not included in the Mg-Pb equilibrium phase diagram proposed in 1985 by Nayeb-Hashemi and Clark, which is now widely spread and used in reference books.[18] More recently, additional studies specially focused on the composition region around Mg_2Pb reinstated the existence of the β' phase.[26,27] However, the crystallographic structure of the latter has not yet been determined with certainty. An orthorhombic $PbCl_2$-type structure (space group *Pnma*, a = 7.50 Å, b = 4.45 Å and c = 8.82 Å) was proposed initially, but has not

been confirmed afterwards.[25] More recently, *ab initio* evolutionary methods were performed and concluded on tetragonal symmetry (space group P4/nmm, a = 4.5396 Å, b = 7.5278 Å).[28] It is interesting to note strong similarities between the XRPD patterns of the non-cubic Mg_2Sn and of this Mg_2Pb polymorph. Therefore, a profile matching refinement with an hexagonal space group was also tried in parallel with the previously mentioned models. However, as in the case of the Mg-Sn system, it was not possible to obtain a clear unique solution, and therefore this compound will be hereafter named "non-cubic Mg_2Pb".

The particle morphology of these intermetallics is shown in insets in Figure 1. Unsurprisingly, the ball-milled powders consists on large aggregates of sub-micrometric particles, as already reported for alloys prepared in similar conditions.[8,29]

The electrochemical behavior of cubic and non-cubic Mg_2Sn and Mg_2Pb is evaluated in half-cell at a significantly higher current rate of C/30. The two first cycles of the four compounds are compared in Figure 2. In both cases, the de-alloying process starts with a stable plateau slightly increasing from 0.25 to 0.3 V before a progressive increase to reach the cut-off value of 0.7 V. With the cubic polymorph of both Mg_2Sn and Mg_2Pb, almost all the magnesium seems to be extracted during the initial charge. After that, the alloying occurs at a low voltage (below 0.2V for Mg_2Sn, below 0.1 V or Mg_2Pb), with a rather limited capacity in both cases that continues upon cycling. Regarding the non-cubic Mg_2Sn and Mg_2Pb polymorphs, the initial electrochemical charge starts similarly to the cubic polymorph with the same plateau potentials. However, in both case the cut-off value is reached more rapidly and induces a capacity reduced by ~50 %.

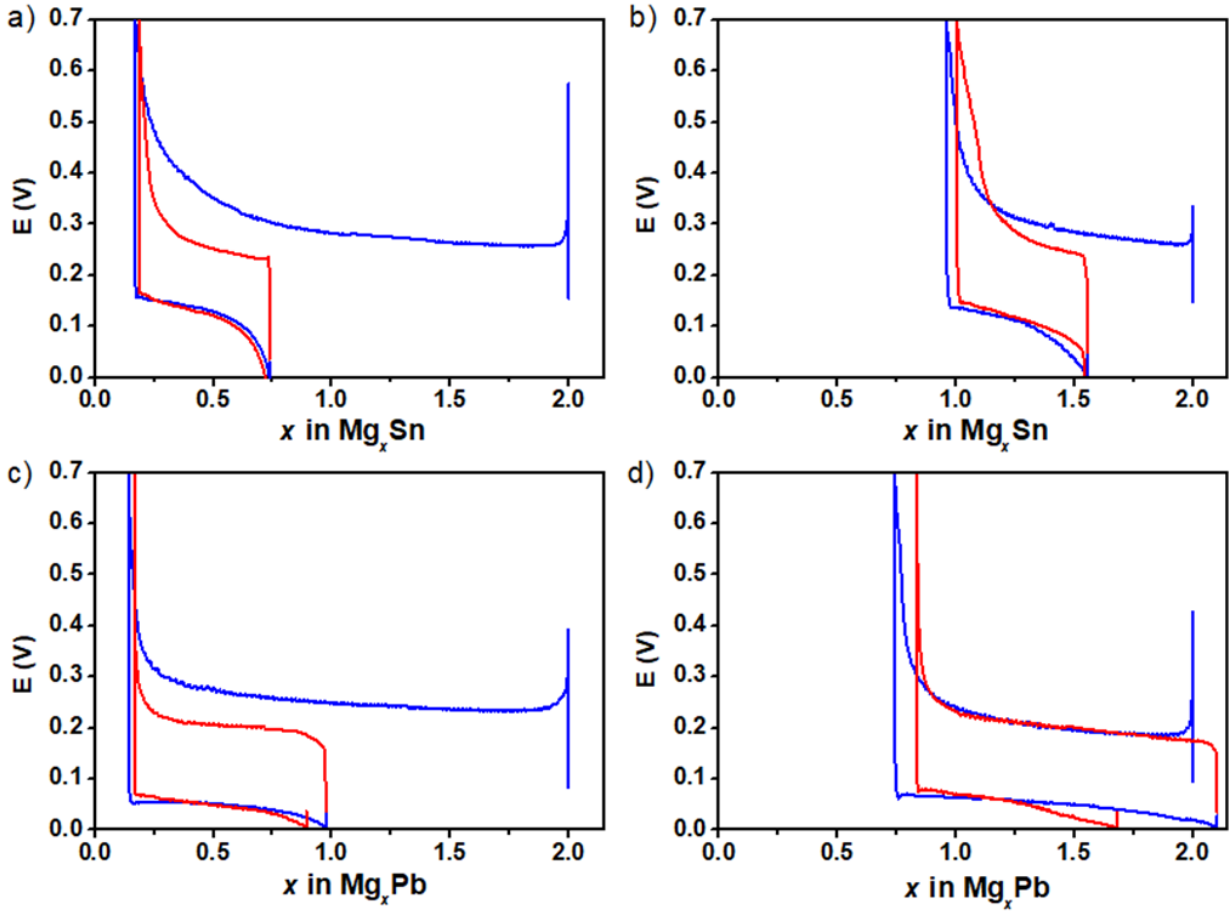

Figure 2: Galvanostatic behavior of Mg/Mg_2Sn and Mg/Mg_2Pb half-cells at C/30 current rate with EtMgCl-Et_2AlCl/THF electrolyte (first cycle in blue, second cycle in red): Mg_2Sn cubic (a) and non-cubic (b), Mg_2Pb cubic (c) and non-cubic (d).

The existing literature on alloy-type materials for Mg-ion batteries clearly underlines that electrodes made from Bi or Mg_3Bi_2 exhibit the best behavior, with especially a limited capacity decay upon cycling with optimized electrode formulation,[7] whereas the cycling performance when starting with Mg_2Sn or Mg_2Pb active materials is somewhat expected to be worse,. The fundamental interest thus lies more on the comparison of the behavior between polymorphs. It is interesting to note that in both case, an almost full electrochemical charge is possible with the cubic polymorphs.

To grasp further details of the electrochemical processes, an *operando* XRD follow-up of the first galvanostatic cycles was carried out for the four polymorphs (Figure 3). Previous *ex situ* XRD patterns collected after magnesiation of tin-based or lead-based electrodes confirmed the formation of the cubic Mg_2Sn and Mg_2Pb, respectively.[11,30] No details, however, were reported about possible intermediates formed along the electrochemical discharge. The de-alloying sequences of the intermetallic compounds are characterized by the disappearance of the peak of each polymorph, while the peaks of tin (β) on one side, or lead on the other side, regularly increase in intensity. This logical observation is in line with the steady-flat voltage plateau characterizing a biphasic alloying reaction.

In case of Mg_2Sn cubic pristine electrode, without any surprise, the subsequent discharge shows the reformation of the cubic Mg_2Sn, the latter exhibiting better crystallinity (narrower diffraction peak at 26.5 ° in Figure 3a). The magnesiation appears more complex in case of the non-cubic pristine electrode: indeed, the beginning of the discharge shows an increase of the diffraction peaks of non-cubic form of Mg_2Sn, followed by a regular increase of the cubic form of Mg_2Sn (Figure 3b). For lead-based electrodes, the early stages of the electrochemical magnesiation are characterized by the appearance of weak reflections that can be assigned to the non-cubic form of Mg_2Pb, whatever the pristine polymorph. As the alloying process continues, these peaks slowly disappear in favor of the cubic form of Mg_2Pb. This unexpected mechanism is better pictured in a top-view plot of the XRPD patterns (Figures S2 to S5). A more detailed analysis of these *operando* XRD studies using a chemometric approach, provided in the supplementary information, globally confirmed the above-mentioned observations, and also provided complementary information on the evolution of the crystallinity between the pristine and electrochemically formed phases (Figures S6 to S16).

For non-cubic Mg_2Pb pristine electrode there is no memory effect that could induce the formation of the non-cubic phase The formation of metastable intermetallic forms during

discharge was already observed during the electrochemical alloying of *p*-block elements, such as antimony, with alkali ions.[31,32] In addition, it is reasonable to assume that the early moments of the electrochemical magnesiation of lead, *i.e.*, when the amount of magnesium is limited, could see the formation of the non-cubic form of Mg_2Pb which is reported to be slightly deficient in magnesium.[25]

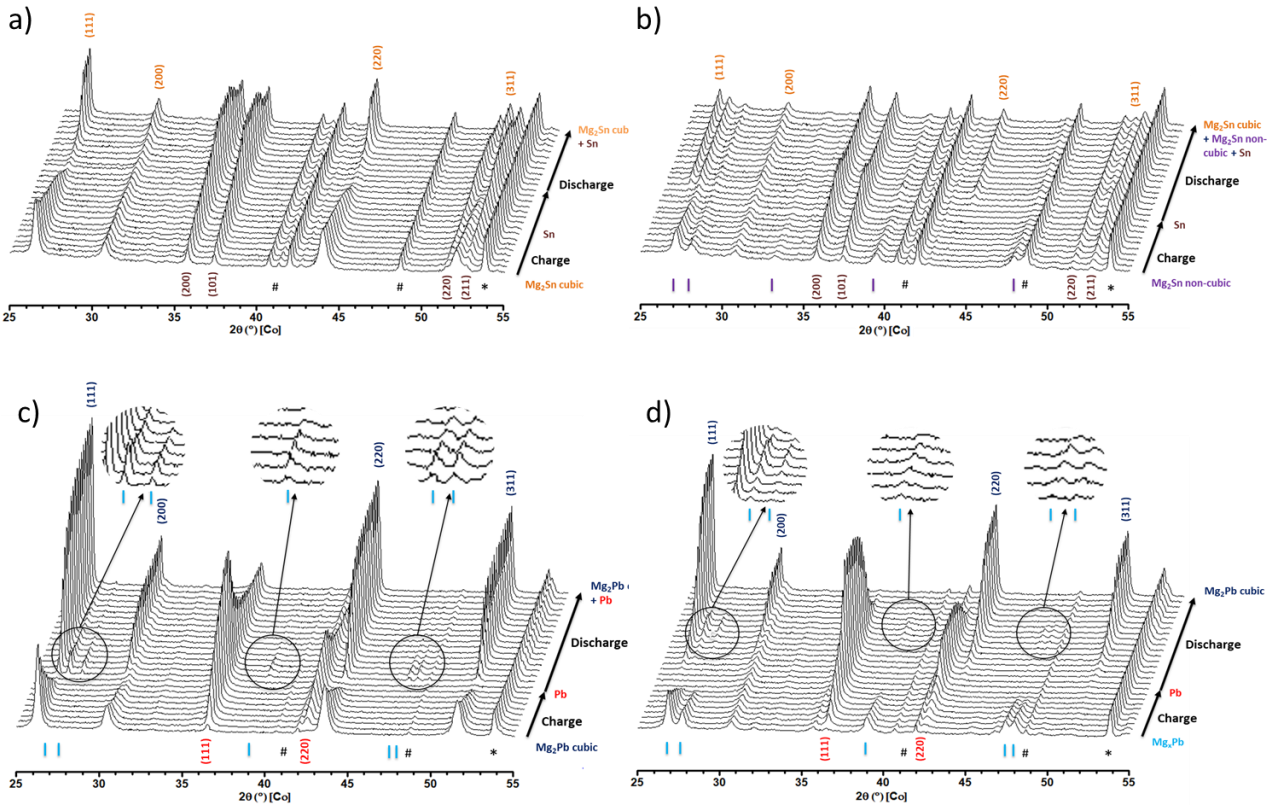

Figure 3: Operando XRPD investigation of the electrochemical behavior of Mg_2Sn cubic (a= and non-cubic (b) and Mg_2Pb (cubic) and non-cubic (d). For each case, peaks indexation or at least Bragg peaks are provided when possible. To enhance the magnesiation process during discharge, a floating was applied once the cell reaches 0 V. Symbols (*) and (#) stand for the beryllium window and unidentified inactive impurities on its surface.

Finally, the compatibility of these intermetallic compounds with $Mg(TFSI)_2$/DME electrolyte in full cells needs to be evaluated. As we previously demonstrated that the cubic forms of

Mg_2Sn and Mg_2Pb *(i)* exhibit the best first capacity during de-alloying process and *(ii)* are mainly formed during electrochemical alloying of both tin and lead forms, only those polymorphs were considered in full Mg-ion cell with Chevrel phase Mo_6S_8 positive electrode materials (Figure 4).

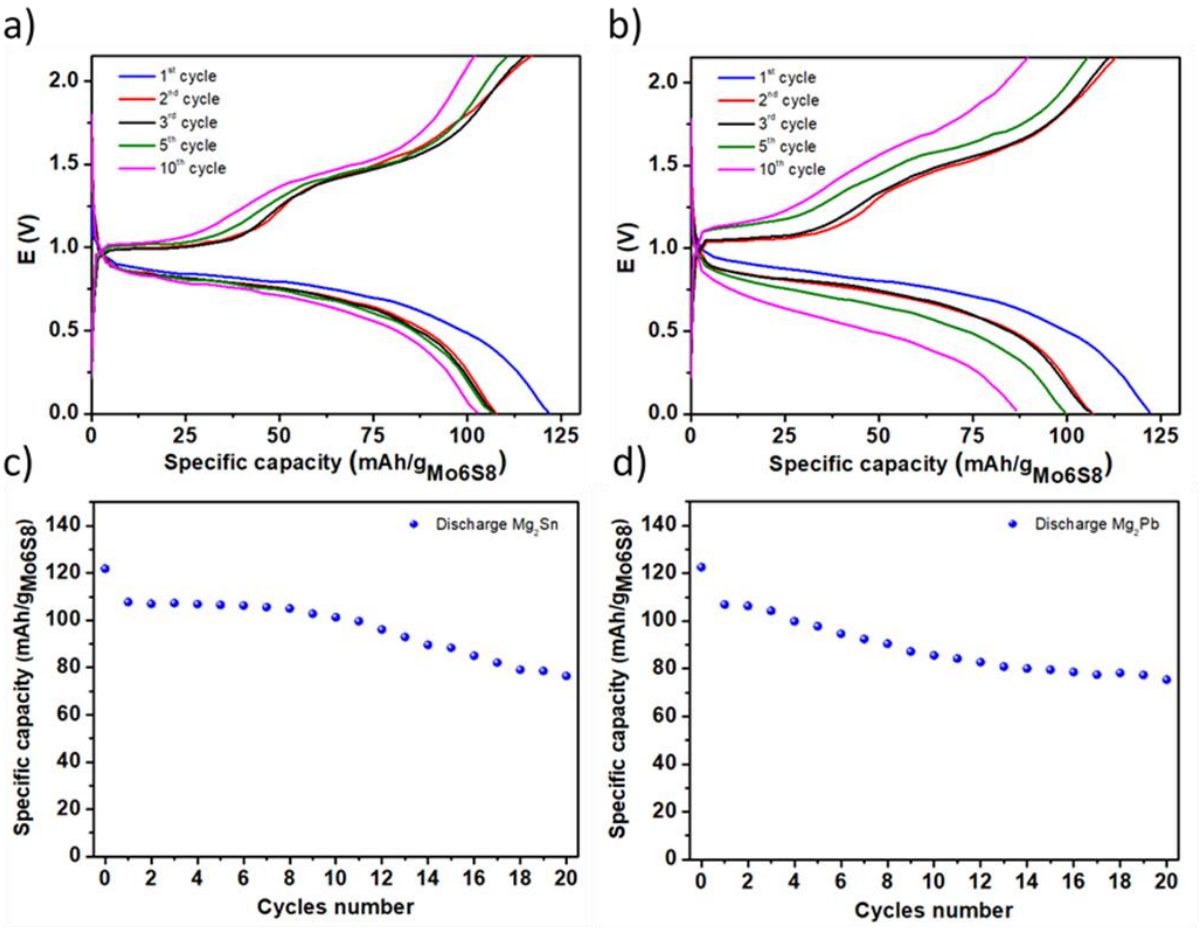

Figure 4: Galvanostatic cycling of full cells Mg_2Sn-cubic/Mo_6S_8 (a) and Mg_2Pb-cubic/Mo_6S_8 (b) at C/10 current rate with $Mg(TFSI)_2$/DME electrolyte, and capacity evolution upon cycling (c and d).

The initial discharge shows a sloppy plateau occurring between 0.8 and 0.5 V for Mg_2Sn, but slightly higher from 0.9 to 0.5 V for Mg_2Pb due to the lower potential of Mg_2Pb below that of Mg_2Sn (respective calculated values of 121 and 197 mV vs. Mg^{2+}/Mg)[33]. During the

corresponding charge, both Mg_2Sn and Mg_2Pb show two plateaus at 1 and 1.4 V that can be attributed to the sequential insertion of Mg^{2+} in the two insertion sites of Mo_6S_8.[34] The differentiation between the two plateaus is not observed on the discharge due to intrinsic kinetic limitations. In both cases, there is a progressive but limited capacity decay upon cycling. The initial capacity loss of 20 mAh/g can be attributed to the partial irreversible magnesium trapping in Mo_6S_8.[35] After that, the progressive loss of capacity may have different origins: first, the degradation of the electrolyte in contact with Mg at low potential can progressively form a blocking layer on the negative electrode.[36] Another possible reason could be the dissolution of the alloying element in the electrolyte and its migration to the positive side that have been observe for Mg_3Bi_2/S batteries.[10] This shuttle phenomenon, which is not yet well understood and could have a negative effect on the cycle life, will be the object of further detailed investigations. Finally, the Mg that is non-reversibly alloy can possibly plate on the negative electrode/electrolyte interface at low potential resulting in the formation of passive Mg and loss of active material.

Conclusions

Different Mg_2Sn and Mg_2Pb allotropes can be prepared by mechanochemical synthesis: besides the cubic forms thermodynamically stable at ambient conditions, this synthetic method allows also obtaining metastable allotropes of these compositions by slightly tuning the milling conditions. The electrochemical evaluation of these phases shows that the first de-magnesiation is almost complete with cubic Mg_2Sn and Mg_2Pb, but only partial with the other polymorphs. *Operando* XRD reveals that, during the following magnesiation, the cubic polymorphs are obtained independent of the pristine polymorph, even though a transient metastable phase is formed at the very beginning of the process in the case of Pb. The compatibility of these phases with $Mg(TFSI)_2$/DME electrolyte when used as negative

electrode materials in Mg-ion batteries was confirmed in Mg_2Sn/Mo_6S_8 and Mg_2Pb/Mo_6S_8 systems. The observed cycle life shows that the behavior of Mg_2Sn and Mg_2Pb as negative electrodes in Mg-ion batteries with a simple $Mg(TFSI)_2$/DME electrolyte are promising regarding the previous studies,[7] and a benchmark in the same electrochemical conditions appears thus necessary to clearly determine the most relevant alloy to be used in magnesium-battery research.

Acknowledgements

The authors gratefully acknowledge financial support from the French National Research Agency (project MISTRALE, ANR-19-CE05-0013, and Labex STORE-EX, ANR-10-LABX-76-01). Access to the Analysis and Characterization platform of "Pôle Chimie Balard" (PAC-Balard) is gratefully acknowledged. Calypso Baril (MEA platform, Univ Montpellier) is acknowledged for the SEM pictures. CIDETEC is acknowledged for providing the C-coated Al foil, with the support of E-Magic FET-PROACTIVE and VIDICAT FET-OPEN projects in the frame of Horizon 2020 Program (Grant agreement 824066 and 829145, respectively).

References

(1) Bonnick, P.; Muldoon, J. A Trip to Oz and a Peak Behind the Curtain of Magnesium Batteries. *Adv. Funct. Mater.* **2020**, *1910510*, 1–15. https://doi.org/10.1002/adfm.201910510.

(2) Dominko, R.; Bitenc, J.; Berthelot, R.; Gauthier, M.; Pagot, G.; Di Noto, V. Magnesium Batteries: Current Picture and Missing Pieces of the Puzzle. *J. Power*

Sources **2020**, *478*. https://doi.org/10.1016/j.jpowsour.2020.229027.

(3) Aurbach, D.; Lu, Z.; Schechter, A.; Gofer, Y.; Gizbar, H.; Turgeman, R.; Cohen, Y.; Moshkovich, M.; Levi, E. Prototype Systems for Rechargeable Magnesium Batteries. *Nature* **2000**, *407* (6805), 724–727.

(4) Pei, C.; Xiong, F.; Yin, Y.; Liu, Z.; Tang, H.; Sun, R.; An, Q.; Mai, L. Recent Progress and Challenges in the Optimization of Electrode Materials for Rechargeable Magnesium Batteries. *Small* **2021**, *17* (3), 2004108. https://doi.org/https://doi.org/10.1002/smll.202004108.

(5) Rashad, M.; Asif, M.; Wang, Y.; He, Z.; Ahmed, I. Recent Advances in Electrolytes and Cathode Materials for Magnesium and Hybrid-Ion Batteries. *Energy Storage Mater.* **2020**, *25*, 342–375. https://doi.org/https://doi.org/10.1016/j.ensm.2019.10.004.

(6) Zhao-Karger, Z.; Fichtner, M. Magnesium-Sulfur Battery: Its Beginning and Recent Progress. *MRS Commun.* **2017**, 1–15.

(7) Niu, J.; Zhang, Z.; Aurbach, D. Alloy Anode Materials for Rechargeable Mg Ion Batteries. **2020**, *2000697*, 1–33. https://doi.org/10.1002/aenm.202000697.

(8) Murgia, F.; Stievano, L.; Monconduit, L.; Berthelot, R. Insight into the Electrochemical Behavior of Micrometric Bi and Mg3Bi2 as High Performance Negative Electrodes for Mg Batteries. *J. Mater. Chem. A* **2015**, *3* (32), 16478–16485.

(9) Tan, Y.-H.; Yao, W.-T.; Zhang, T.; Ma, T.; Lu, L.-L.; Zhou, F.; Yao, H.-B.; Yu, S.-H. High Voltage Magnesium-Ion Battery Enabled by Nanocluster Mg3Bi2 Alloy Anode in Noncorrosive Electrolyte. *ACS Nano* **2018**, *12* (6), 5856–5865. https://doi.org/10.1021/acsnano.8b01847.

(10) Meng, Z.; Foix, D.; Brun, N.; Dedryvère, R.; Stievano, L.; Morcrette, M.; Berthelot, R.

Alloys to Replace Mg Anodes in Efficient and Practical Mg-Ion/Sulfur Batteries. *ACS Energy Lett.* **2019**, *4* (9), 2040–2044. https://doi.org/10.1021/acsenergylett.9b01389.

(11) Singh, N.; Arthur, T. S.; Ling, C.; Matsui, M.; Mizuno, F. A High Energy-Density Tin Anode for Rechargeable Magnesium-Ion Batteries. *Chem. Commun.* **2013**, *49* (2), 149–151.

(12) Nguyen, D.; Song, S. Magnesium Stannide as a High-Capacity Anode for Magnesium-Ion Batteries. *J. Power Sources* **2017**, *368*, 11–17. https://doi.org/10.1016/j.jpowsour.2017.09.054.

(13) Nguyen, G. T. H.; Nguyen, D.-T.; Song, S.-W. Unveiling the Roles of Formation Process in Improving Cycling Performance of Magnesium Stannide Composite Anode for Magnesium-Ion Batteries. *Adv. Mater. Interfaces* **2018**, *5* (22), 1801039. https://doi.org/https://doi.org/10.1002/admi.201801039.

(14) Periyapperuma, K.; Tran, T. T.; Purcell, M. I.; Obrovac, M. N. The Reversible Magnesiation of Pb. *Electrochim. Acta* **2015**, *165* (0), 162–165.

(15) Chusid, O.; Gofer, Y.; Gizbar, H.; Vestfrid, Y.; Levi, E.; Aurbach, D.; Riech, I. Solid-State Rechargeable Magnesium Batteries. *Adv. Mater.* **2003**, *15* (7–8), 627–630.

(16) Morcrette, M.; Chabre, Y.; Vaughan, G. B. M.; Amatucci, G. G.; Leriche, J.-B.; Patoux, S.; Masquelier, C.; Tarascon, J.-M. In Situ X-Ray Diffraction Techniques as a Powerful Tool to Study Battery Electrode Materials. *Electrochim. Acta* **2002**, *47* (19), 3137–3149. https://doi.org/10.1016/S0013-4686(02)00233-5.

(17) Nayeb-Hashemi, A. A.; Clark, J. B. The Mg-Sn (Magnesium-Tin) System. *Bull. Alloy Ph. Diag.* **1984**, *5* (6), 466–476. https://doi.org/10.1007/BF02868320.

(18) Nayeb-Hashemi, A. A.; Clark, J. B. The Mg-Pb (Magnesium-Lead) System. *Bull. Alloy*

Phase Diagrams **1985**, *6* (1), 123–124.

(19) Cannon, P.; Conlin, E. T. Magnesium Compounds: New Dense Phases. *Science (80-.).* **1964**, *145* (3631), 487 LP – 489. https://doi.org/10.1126/science.145.3631.487.

(20) Dyuzheva, T. I.; Bendeliani, N. A.; Dzhavadov, L. N.; Kolobyanina, T. N.; Nikolaev, N. A. Crystal Growth of the High-Pressure Phase of Mg2Sn. *J. Alloys Compd.* **1995**, *223* (1), 74–76. https://doi.org/https://doi.org/10.1016/0925-8388(94)01441-8.

(21) Urretavizcaya, G.; Meyer, G. O. Metastable Hexagonal Mg2Sn Obtained by Mechanical Alloying. *J. Alloys Compd.* **2002**, *339* (1), 211–215. https://doi.org/https://doi.org/10.1016/S0925-8388(01)02001-1.

(22) Range, K.-J.; Grosch, G. H.; Andratschke, M. Studies on AB2-Type Intermetallic Compounds. Part V1. The Crystal Structure of Mg9Sn5, a Supposed High-Pressure Modification of Mg2Sn. *J. Alloys Compd.* **1996**, *244* (1), 170–174. https://doi.org/https://doi.org/10.1016/S0925-8388(96)02432-2.

(23) Clark, C. R.; Wright, C.; Suryanarayana, C.; Baburaj, E. G.; Froes, F. H. Synthesis of Mg2X (X = Si, Ge, or Sn) Intermetallics by Mechanical Alloying. *Mater. Lett.* **1997**, *33* (1), 71–75. https://doi.org/https://doi.org/10.1016/S0167-577X(97)00081-5.

(24) Suganuma, R. A Metastable Phase in Sn-Mg Alloy Film. *J. Phys. Soc. Japan* **1959**, *14* (5), 685–686. https://doi.org/10.1143/JPSJ.14.685.

(25) Eldrige, J.; Miller, E.; Komarek, K. Magnesium-Lead Phase Diagram and Activity of Magnesium of Liquid Magnesium-Lead Alloys. *Trans. Met. Soc. AIME* **1965**, *233*, 1303.

(26) Siviour, N. G.; Ng, K. Mg-Pb Phase Diagram and Phase Transformations in the Intermetallic Compounds Mg2Pb and β. *Metall. Mater. Trans. B* **1994**, *25* (2), 265–

275. https://doi.org/10.1007/BF02665209.

(27) Stankus, S. V; Khairulin, R. A. Density and Phase Diagram of the Magnesium–Lead System in the Region of Mg2Pb Intermetallic Compound. *Thermochim. Acta* **2008**, *474* (1), 52–56. https://doi.org/https://doi.org/10.1016/j.tca.2008.05.011.

(28) Li, Y.; Bian, G.; Singh, D. J. Identification and Properties of the Non-Cubic Phases of Mg2Pb. *AIP Adv.* **2016**, *6* (12), 125108. https://doi.org/10.1063/1.4972957.

(29) Murgia, F.; Weldekidan, E. T.; Stievano, L.; Monconduit, L.; Berthelot, R. First Investigation of Indium-Based Electrode in Mg Battery. *Electrochem. Commun.* **2015**, *60*, 56–59. https://doi.org/10.1016/j.elecom.2015.08.007.

(30) Periyapperuma, K.; Tran, T. T.; Purcell, M. I.; Obrovac, M. N. The Reversible Magnesiation of Pb. *Electrochim. Acta* **2015**, *165*, 162–165. https://doi.org/10.1016/j.electacta.2015.03.006.

(31) Darwiche, A.; Marino, C.; Sougrati, M. T.; Fraisse, B.; Stievano, L.; Monconduit, L. Better Cycling Performances of Bulk Sb in Na-Ion Batteries Compared to Li-Ion Systems: An Unexpected Electrochemical Mechanism. *J. Am. Chem. Soc.* **2012**, *134*, 20805–20811.

(32) Allan, P. K.; Griffin, J. M.; Darwiche, A.; Borkiewicz, O. J.; Wiaderek, K. M.; Chapman, K. W.; Morris, A. J.; Chupas, P. J.; Monconduit, L.; Grey, C. P. Tracking Sodium-Antimonide Phase Transformations in Sodium-Ion Anodes: Insights from Operando Pair Distribution Function Analysis and Solid-State NMR Spectroscopy. *J. Am. Chem. Soc.* **2016**, *138* (7), 2352–2365. https://doi.org/10.1021/jacs.5b13273.

(33) Gerstein, B. C.; Jelinek, F. J.; Habenschuss, M.; Shickell, W. D.; Mullaly, J. R.; Chung, P. L. Thermal Study of Groups II—IV Semiconductors. Lattice Heat Capacities and

Free Energies of Formation. Heat Capacity of Mg2Si from 15°—300°K. *J. Chem. Phys.* **1967**, *47* (6), 2109–2115. https://doi.org/10.1063/1.1712243.

(34) Mei, L.; Xu, J.; Wei, Z.; Liu, H.; Li, Y.; Ma, J.; Dou, S. Chevrel Phase Mo6T8 (T = S, Se) as Electrodes for Advanced Energy Storage. *Small* **2017**, *13* (34), 1701441. https://doi.org/10.1002/smll.201701441.

(35) Ling, C.; Suto, K. Thermodynamic Origin of Irreversible Magnesium Trapping in Chevrel Phase Mo6S8: Importance of Magnesium and Vacancy Ordering. *Chem. Mater.* **2017**, *29* (8), 3731–3739. https://doi.org/10.1021/acs.chemmater.7b00772.

(36) Kopač Lautar, A.; Bitenc, J.; Rejec, T.; Dominko, R.; Filhol, J. S.; Doublet, M. L. Electrolyte Reactivity in the Double Layer in Mg Batteries: An Interface Potential-Dependent DFT Study. *J. Am. Chem. Soc.* **2020**, *142* (11), 5146–5153. https://doi.org/10.1021/jacs.9b12474.

Supporting Information for:

Electrochemical behavior of Mg_2Sn and Mg_2Pb polymorphs in Mg-ion batteries

Submission to Journal of Magnesium and Alloys

Clément Pechberty, Antoine Klein, Bernard Fraisse, Lorenzo Stievano, Romain Berthelot*

ICGM, Univ Montpellier, CNRS, ENSCM, Montpellier, France

RS2E, CNRS, Hub de l'Energie, Amiens, France

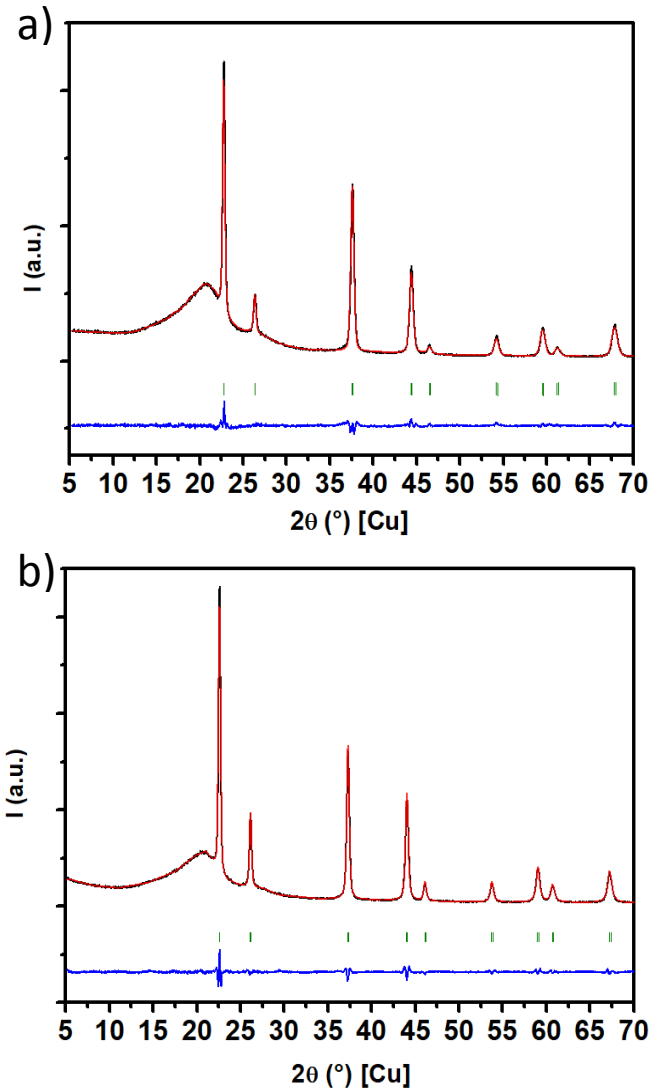

Figure S1: XRD patterns of cubic Mg2Sn (a) and Mg2Pb (b) with profile matching refinement.

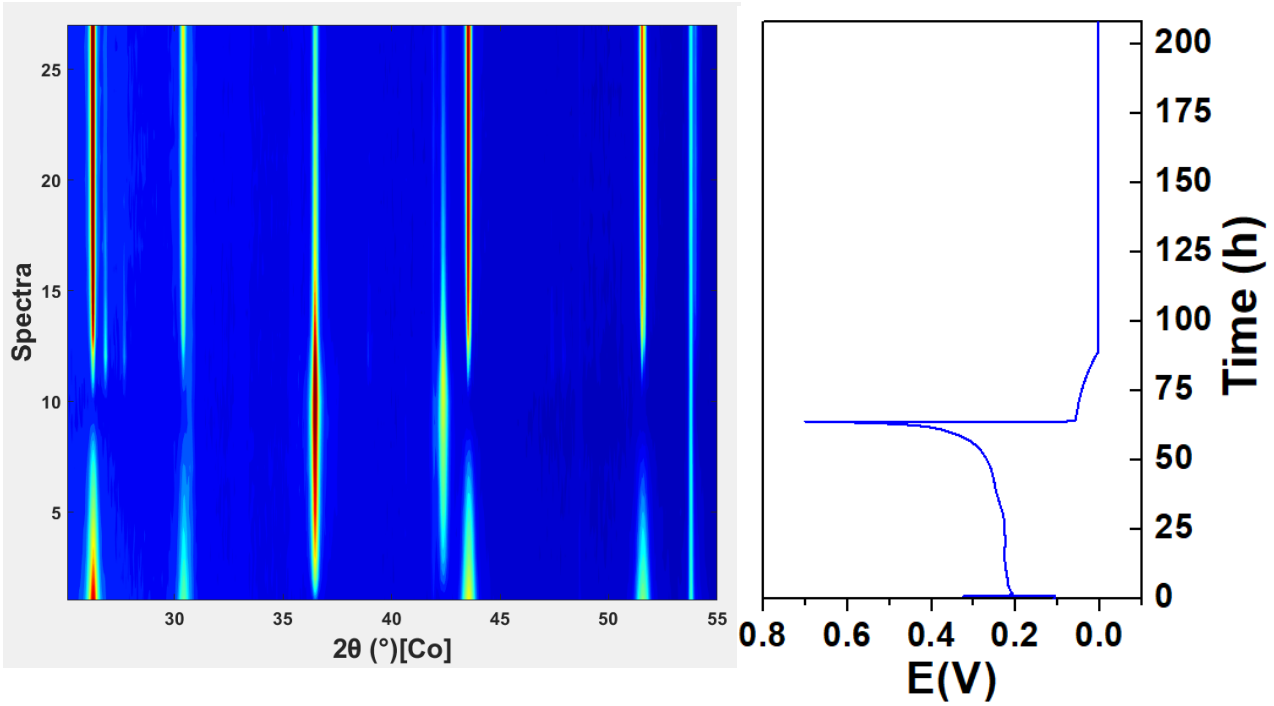

Figure S2: Top view of the operando XRD patterns measured during a full demagnesiation-magnesiation cycle of cubic Mg_2Pb and corresponding electrochemical signature.

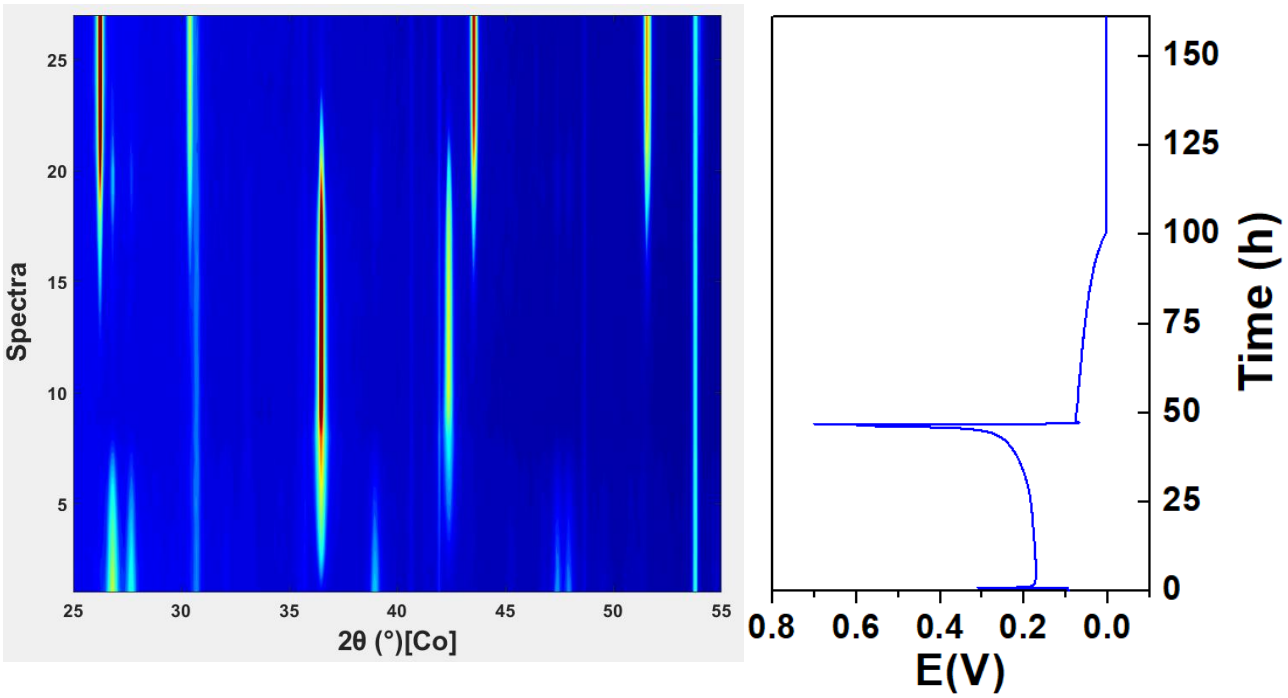

Figure S3: Top view of the operando XRD patterns measured during a full demagnesiation-magnesiation cycle of non-cubic Mg_2Pb and corresponding electrochemical signature.

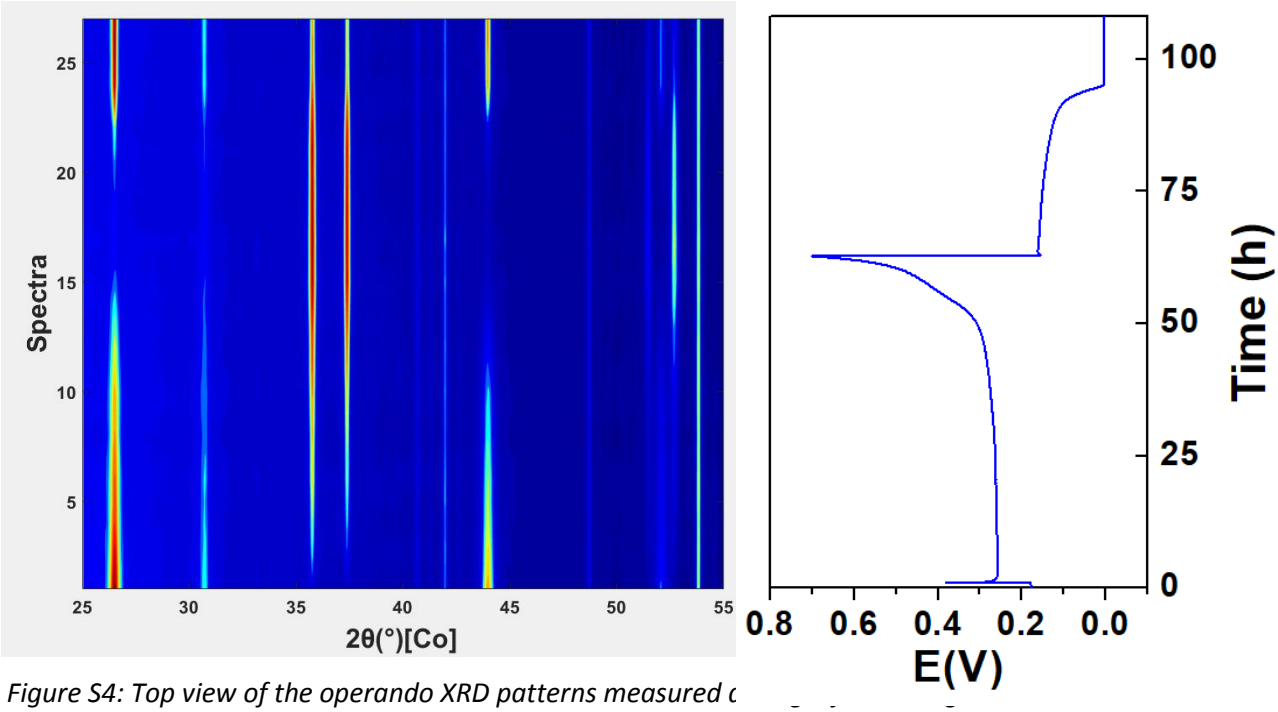

Figure S4: Top view of the operando XRD patterns measured d
magnesiation cycle of cubic Mg_2Sn and corresponding electrochemical signature.

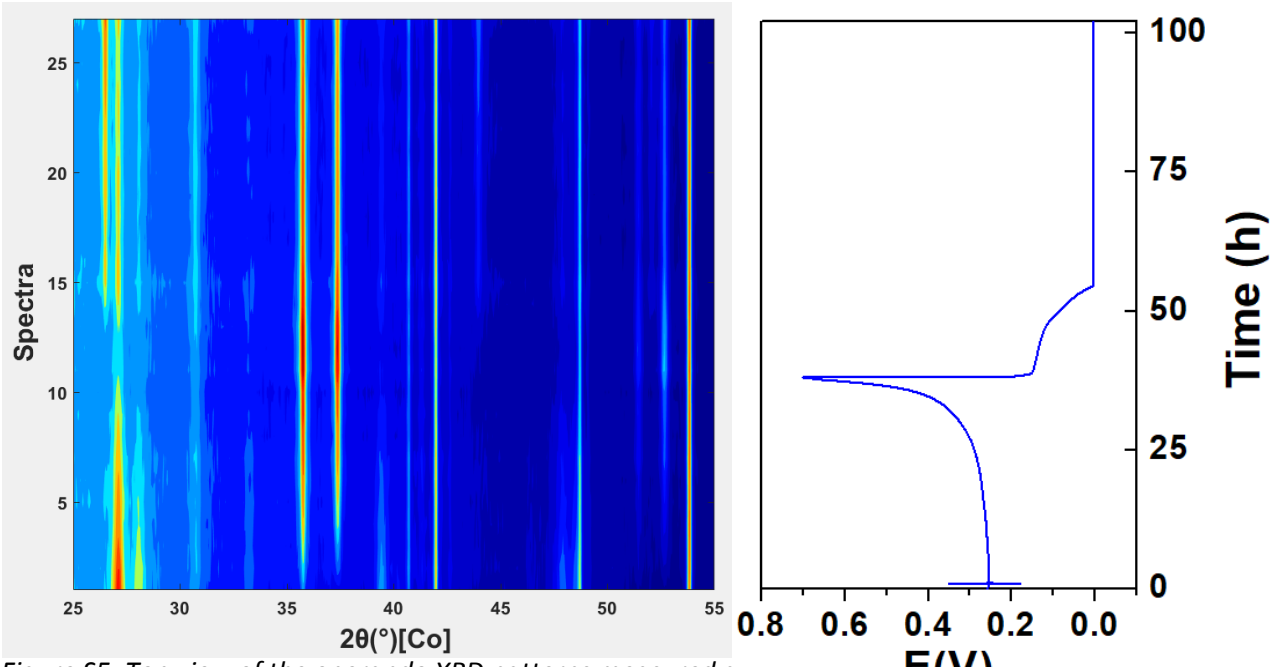

Figure S5: Top view of the operando XRD patterns measured d
magnesiation cycle of non-cubic Mg_2Sn and corresponding electrochemical signature.

Chemometric analysis of the X-ray diffraction (XRD) patterns

A common chemometric approach based on Principal Component Analysis (PCA) was applied to determine the minimum number of components expressing the variance included in the whole set of *operando* XRD data. The analysis was carried out separately for the four *operando* datasets. PCA is a factor analysis tool typically used to structure and simplify complex data sets by narrowing the multitude of variables with the least number of independent components.[1] In this specific case, this corresponds to the number of different XRD patterns necessary to express, by appropriate linear combinations, each dataset collected during a full electrochemical demagnesiation-magnesiation cycle.

The number of principal components determined in this way can be used as the basis for Multivariate Curve Resolution-Alternating Least Squares (MCR-ALS) analysis. This algorithm allows the stepwise reconstruction of the "pure" components that are necessary for interpreting the whole *operando* multiset. The whole procedure is described in detail in ref. [2]. The MCR-ALS analysis was performed with the following constraints: (i) non-negativity of the intensity and of the concentration of the components, (ii) no unimodality and (iii) closure (sum of the components always equal to 100 % of the intensity). In this way, the different patterns which are necessary reproduce by the linear combination the whole dataset are obtained. The results of the application of this process is detailed below for the four *operando* XRD datasets collected during a full electrochemical demagnesiation-magnesiation cycle of cubic and non-cubic Mg_2Pb and Mg_2Sn. In order to help this analysis to converge to reasonable values, a linear background was subtracted to all patterns in order to bring the baseline at 0 before applying PCA and MCR-ALS.

Cubic Mg_2Pb

The results of the PCA analysis of the *operando* XRD data measured for Mg_2Pb are collected in Figure S6. By inspection of the variance plot and of the shape sand evolution of the different components, four to five independent components are necessary to express the whole dataset.

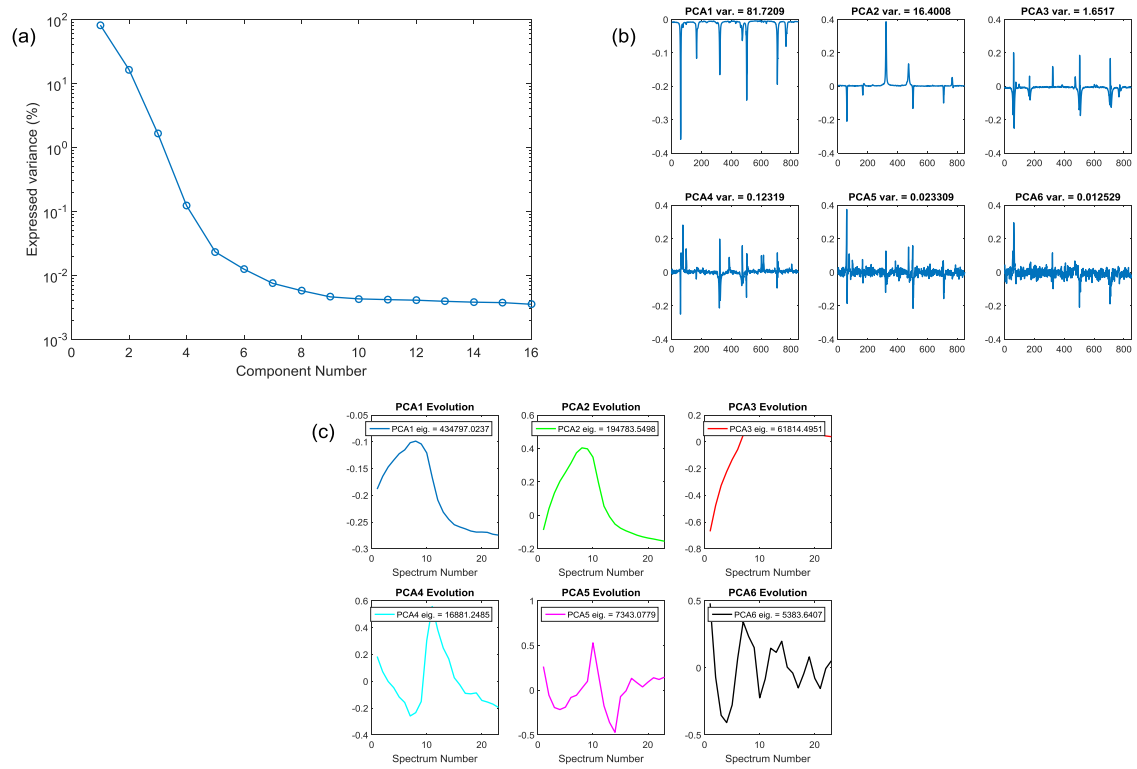

Figure S6: Variance plot (a), principal components (b) and the evolution of their contribution (c) along the full demagnesiation-magnesiation cycle of cubic Mg_2Pb.

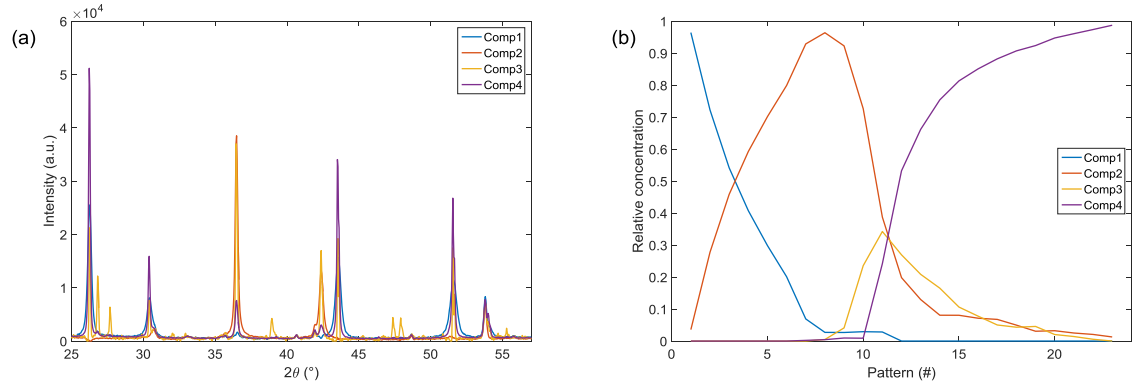

Figure S7: Pure components (a) and evolution of their concentration (c) along the full demagnesiation-magnesiation cycle of cubic Mg_2Pb.

The application of MCR-ALS provides sufficiently good results using four independent components, as shown in Figure S7. In this case, components 1 and 4 Correspond to the same phase, *i.e.*, cubic Mg_2Pb, but are differentiated by a strong modification of the line shape and width: component 4 has a much narrower shape, corresponding to the reversible formation of sensibly smaller crystallites at the end of a full electrochemical cycle. Component 2 corresponds to pure Pb metal, whereas component 3 has contributions from both cubic Mg_2Pb and Pb metal, but contains also additional reflections corresponding to the pattern of non-cubic Mg_2Pb. In this last component, all linewidths are very narrow, corresponding to well-crystallised phases. By looking at the evolution of their

concentration, one can thus quite straightforwardly understand the reaction mechanisms occurring along the demagnesiation and the following magnesiation. The first process is the biphasic transformation of non-cubic Mg_2Pb into Pb. At the beginning of the following discharge, both non-cubic and cubic well-crystallised Mg_2Pb appear at the beginning, at the expenses of the smaller crystallites of Mg_2Pb. Non-cubic Mg_2Pb reaches a maximum in the course of the discharge and then disappears completely, leaving the place to the cubic form, which is the only phase detected at the end of the magnesiation.

Non-cubic Mg_2Pb

The results of the PCA analysis of the *operando* XRD data measured for non-cubic Mg_2Pb are collected in Figure S8. By inspection of the variance plot and of the shape sand evolution of the different components, four to five independent components are necessary to express the whole dataset.

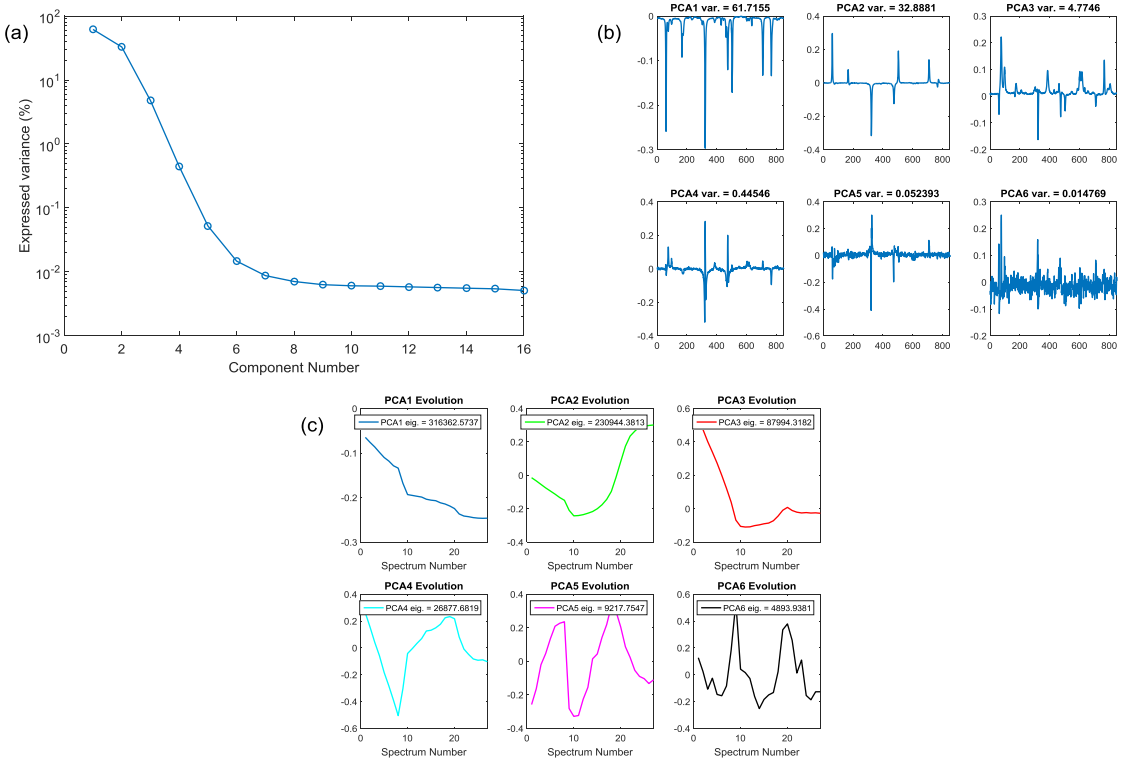

Figure S8: Variance plot (a), principal components (b) and the evolution of their contribution (c) along the full demagnesiation-magnesiation cycle of non-cubic Mg_2Pb.

The application of MCR-ALS provides good results using four independent components, as shown in Figure S9. In this case, components 1 and 4 can be easily indexed as non-cubic and cubic Mg_2Pb, respectively, while both intermediate components 2 and 3 correspond to Pb metal, with however different profile shapes: component 2 has a larger linewidth, corresponding to smaller crystallites. By looking at the evolution of their concentration, one can then easily describe the sequence of

processes occurring along the demagnesiation and the following magnesiation. The first process is the biphasic transformation of non-cubic Mg_2Pb into small particles of Pb, which grow towards the end of the charge, corresponding to pattern #11. During the following discharge, both non-cubic and cubic Mg_2Pb appear at the beginning, but the former, metastable, reaches a maximum after transforming back to the cubic form, which is the only phase detected at the end of the magnesiation.

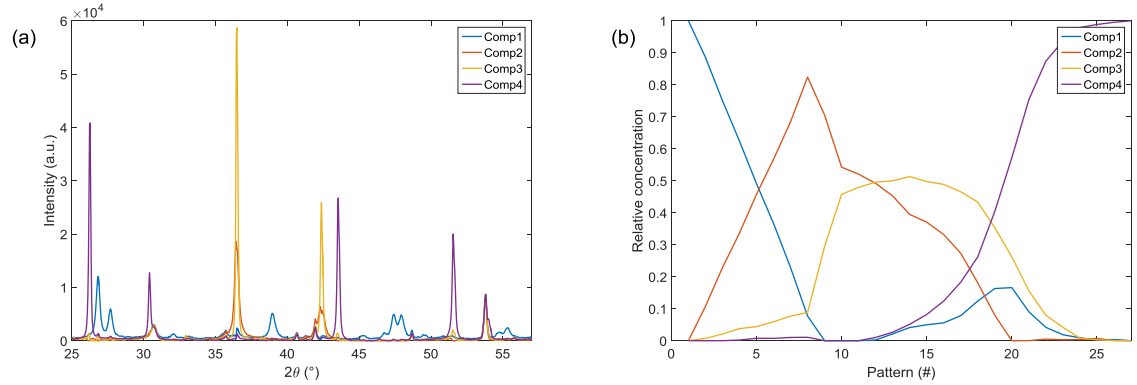

Figure S9: MCR-ALS pure components (a) and the evolution of their concentration (c) along the full demagnesiation-magnesiation cycle of non-cubic Mg_2Pb.

Cubic Mg_2Sn

The results of the PCA analysis of the *operando* XRD data measured for cubic Mg_2Sn are collected in Figure S10. By inspection of the variance plot and of the shape sand evolution of the different components, three independent components are necessary to express the whole dataset.

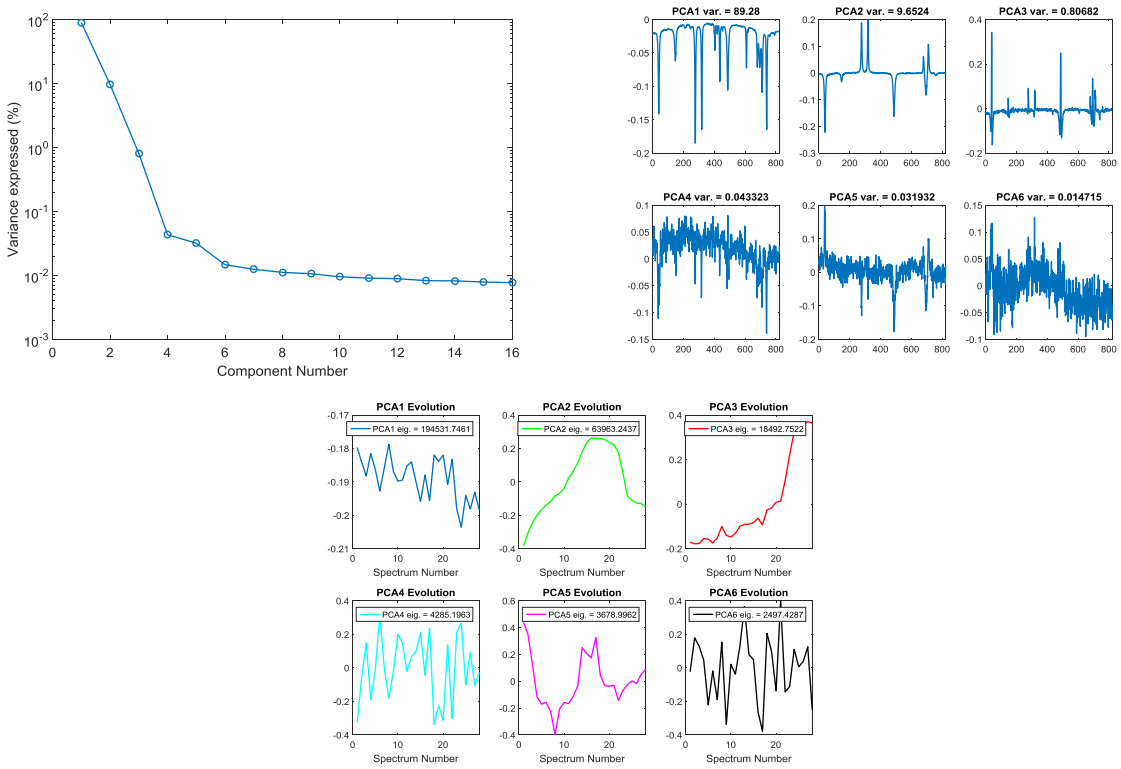

Figure S10: Variance plot (a), principal components (b) and the evolution of their contribution (c) along the full demagnesiation-magnesiation cycle of cubic Mg_2Sn.

The application of MCR-ALS provides good results using three independent components, as shown in Figure S11. In this case, components 1 and 3 can be both indexed as cubic Mg_2Sn, respectively, components 2 corresponds to β-Sn metal. Components 1 and 3 are differentiated by a different profile shape: component 1 has a larger linewidth, corresponding to smaller crystallites. These three components describe a sequence of two simple biphasic mechanisms, with cubic Mg_2Sn transforming into Sn during the charge, and then transforming back to cubic Mg_2Sn with higher crystallinity during the following discharge. This transformation is not completed at the end of the latter process, where only half of the tin is transformed back into Mg_2Sn

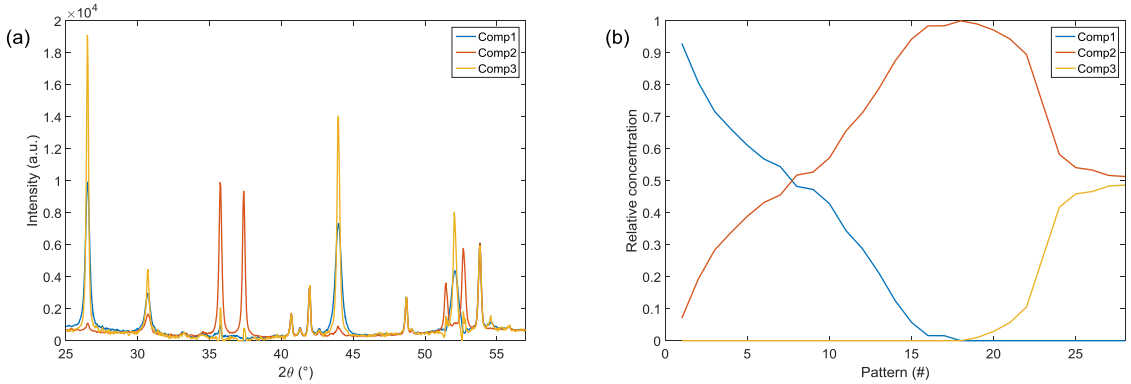

Figure S11: MCR-ALS pure components (a) and the evolution of their concentration (c) along the full demagnesiation-magnesiation cycle of cubic Mg_2Sn.

Non-cubic Mg_2Sn

The results of the PCA analysis of the *operando* XRD data measured for non-cubic Mg_2Sn are collected in Figure S12. By inspection of the variance plot and of the shape sand evolution of the different components, three independent components are necessary to express the whole dataset.

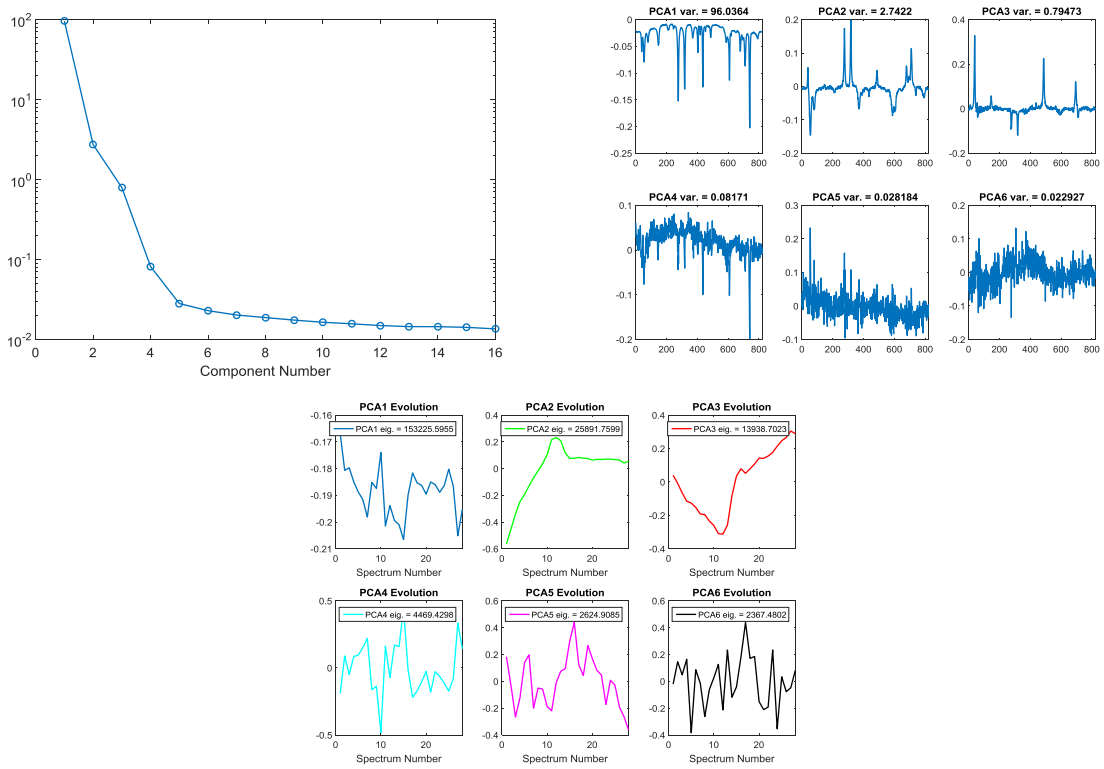

Figure S12: Variance plot (a), principal components (b) and the evolution of their contribution (c) along the full demagnesiation-magnesiation cycle of non-cubic Mg_2Sn.

The application of MCR-ALS with three independent components provides a good reconstruction of the pure components, as shown in Figure S13. In this case, components 1 can be indexed as the pristine non-cubic Mg_2Sn, while component 2 corresponds to β-Sn metal. A direct and complete transformation of the first component into the second one is obtained along the first charge, corresponding to the full demagnesiation of non-cubic Mg_2Sn. During the charge, the formation of components 3 occurs: this component is rather interesting, since it contains at the same time the contributions of non-cubic Mg_2Sn and cubic Mg_2Sn, the former better crystallised than the pristine material represented by component 1. The fact that both phases are contained in the same component suggest that both phases are formed at the same rate during the discharge, and that, differently from the case of non-cubic Mg_2Pb shown above, the non-cubic Mg_2Sn reformed during magnesiation does not transform into the cubic form. The charge, however, is not complete, and a majority of tin metal is still present at the end of the process.

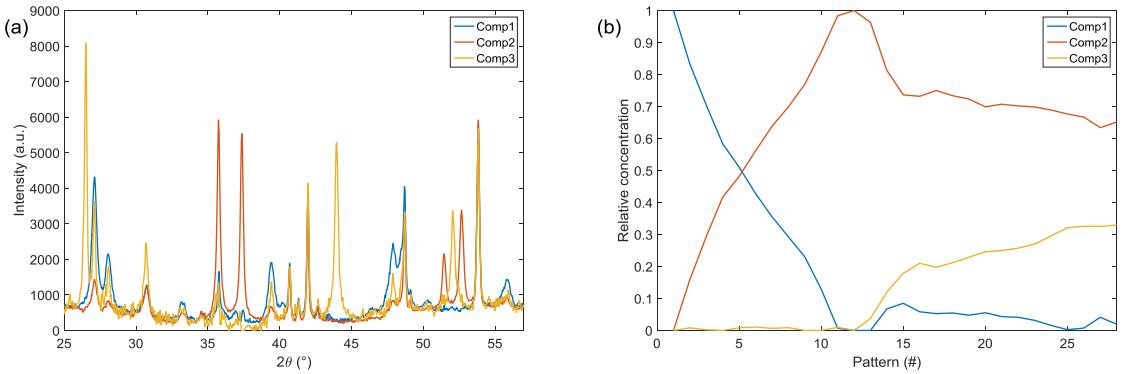

Figure S13: MCR-ALS pure components (a) and the evolution of their concentration (c) along the full demagnesiation-magnesiation cycle of cubic Mg_2Sn.

References

[1] D.L. Massart, B.G.M. Vandeginste, L.M.C. Buydens, S. De Jong, P.J. Lewi, J. Smeyers-Verbeke, Handbook of Chemometrics and Qualimetrics: Part A, 1st Editio, Elsevier B.V., Amsterdam, 1997. https://www.elsevier.com/books/handbook-of-chemometrics-and-qualimetrics/massart/978-0-444-89724-4.

[2] M. Fehse, A. Iadecola, M.T. Sougrati, P. Conti, M. Giorgetti, L. Stievano, Applying chemometrics to study battery materials: Towards the comprehensive analysis of complex operando datasets, Energy Storage Mater. 18 (2019) 328–337. doi:10.1016/j.ensm.2019.02.002.